ORIGINAL ARTICLE

Sealing of Porous Anodic Film by Cerium-Conversion Coating on AA2024 Aluminum Alloy: Study on the Anticorrosion Performance

S. Zeghaoui[1] · Z. Hanniche[2] · I. Bouyakoub[2] · H. Yousfi[1] · A. Abdi[2] · M. Trari[3]

Abstract

In this study, we report investigation on the synergistic effect efficiency between anodizing process and cerium-based conversion deposit (CeEC) on the corrosion behavior of 2024-T4 aluminum alloy substrate. Structural and chemical details were revealed by the X-ray diffraction (XRD) and Raman microscopy. The synergistic effect efficiency against corrosion of 2024 Al-alloy in contact with aerated 3.5 wt.% NaCl solution was clearly evidenced from the potentiodynamic polarization technique and electrochemical impedance spectroscopy (EIS), over a wide frequency domain (1 MHz–1 mHz). The polarization resistance ($> 10^5 \, k\Omega \, cm^2$) and the inhibiting efficiency ($> 97\%$) obtained for the Al-alloy specimen undergoing both anodizing and CeEC deposit reveal outstanding anticorrosion properties, in contrast to the CeEC-treated and untreated samples.

1 Introduction

The 2024 aluminum alloy (Al-2024) is an important engineering material for many applications requiring a high strength to weight ratio and good resistance to fatigue, such as aviation and aerospace industries, automotive, truck wheels, rivets and other applications [1–3]. However, it was reported that for Al-2024, containing Cu and Mg [4–6], the presence of intermetallic precipitations, produced during age-strengthening treatments for improving mechanical properties, such as S–Al$_2$CuMg, reduces considerably the resistance against corrosion. Localized corrosion occurs mainly as pitting and intergranular corrosion, and initiating at discrete sites in the vicinity of the Cu-rich intermetallic phases. For many years, chromium (VI)-based chemical conversion coatings (CHC) were widely used as a final finish pretreatment for improving the corrosion resistance of aluminum and its alloys [7]. Cr(VI) is hazardous for the human health and environment, even at very low concentrations [8,

9], the rare-earth conversion coatings (REE) are promising to the CHC treatments [10–12]. Two methods are commonly used for preparing the REEs of the cleaned and pre-treated metal surface in a salt solution at a definite conversion conditions, such as pH and temperature, to develop a protective barrier that will remain chemically bonded to the substrate; the chemical conversion coating (CC) and the electrochemical conversion coating (EC), using a cathodic polarization [13].

Among the REEs, cerium-based conversion coating (CeEC) using cathodic polarization attracts much attention owing to their adherent oxides/hydroxides deposits conferring a significant inhibition effect against the localized corrosion [14–20], and providing a high stability against mechanical abrasion [21]. Another successful technique, which was applied to different classes of Al-alloy, is the aluminum anodizing process (AAP) [22], whose performance is improved by various sealing processes, involving a hot deionized water or bath containing metal salts [23–28]. More recently, Catalina et al. [29] have successfully investigated the polypyrrole deposition on hard anodized coatings of the aluminum alloy 2024-T3. However, to our knowledge, until now there is no reported studies about the synergistic effect between the electrochemical conversion coating performed in aqueous media and the AAP. For this purpose, the aim of this work is to investigate the synergetic effect of combined electrochemical Ce-conversion coating and anodizing

✉ M. Trari
solarchemistry@gmail.com; mtrari@usthb.dz

1 Ecole Nationale Polytechnique, 16200 Algiers, Algeria

2 Laboratoire d'Electrochimie Et de Corrosion, Ecole Militaire Polytechnique, BP 17, 16111 Algiers, Algeria

3 LSVER, USTHB, BP 32, 16111 Algiers, Algeria

treatments on the corrosion protection of the 2024-T4 Al alloy in a chloride-rich aerated environment (3.5 wt.%).

2 Experimentation

The purity of all products (Alfa Aesar Company) was higher than 99% and solutions were prepared in distilled water (~ 0.8 MΩ cm). Rectangular specimens (1 cm^2) of 2024 Al alloy were used as substrates. The XRF analysis indicates the following composition (in wt. %): 4.942 Cu, 0.5 Fe, 1.8 Mg, 0.1 Cr, 0.25 Zn, 0.5 Si, 0.9 Mn, 0.15 Ti and balance of Al were used.

To remove compressive and tensile residual stress, The Al samples were annealed at 300 °C for 30 min and cooled at room temperature for 3 days. Then, it has undergone T4-natural ageing treatment in a programmable electric furnace, involving firstly a solution treated at 530 °C for 55 min, followed by a rapid quenching in water at room temperature, then natural aged at 20 °C for 20 days under air.

2.1 Ce-Conversion Coating and Anodizing Procedures

All samples are subjected to a mechanical polishing by 400 and 800 grit emery papers, degreased in acetone and ethanol and air dried. They were etched in 10 g/L NaOH at 65 °C (3 min), dipped in acid cleaning solution (H$_2$CrO$_4$ 60 g/L, H$_2$SO$_4$ 180 mL/L) at 65 °C to neutralize any residual alkali, and finally rinsed abundantly with distilled water. Specimens were divided into groups; the first one (G1) was subject to a CeEC treatment using the galvanostatic cathodic polarization (GCP) method in M CeCl$_3$.7H$_2$O (0.1 M), under current densities of 2.5, 5, 7.5 and 10 mA/cm^2 over 5, 10, 15 and 30 min, to determine the optimal treatment parameters. The second group (G2) was anodized and treated by cerium-conversion coating (An/CeEC) under optimal conditions to emphasize the synergistic effect between them. The anodizing process was achieved using a DC-power supply in a conventional two-electrode system containing 18wt.% H$_2$SO$_4$, at 1.5 A/cm^2 and 30 min, to obtain alumina layer thickness of 17.2 μm; a rectangular lead plate has been used as cathode. Afterwards, all samples were rinsed with water and acetone and air-dried. All experiments were performed at a fixed temperature of 25 °C and repeated at least three times.

2.2 Characterization

The composition of the 2024 aluminum specimen was analyzed by X-Ray fluorescence using EDX—800HS spectrometer. The structural characterization of the elaborated layers was elucidated by X-ray diffraction (XRD) using a Bruker D8 Advance Powder diffractometer (CuK$_\alpha$ radiation, $\lambda = 1.54056$ Å) over the 2θ range (10—120°), with a step size of 0.05° and a scan time of 1.5 s per step (scan rate of 2° min^{-1}). More information about the molecular structure and morphology were provided thanks to a Thermo Fisher DXR Raman microscope by focusing a high laser beam at 532 nm in the wave number range (100–2000 cm^{-1}). The thickness of the oxide layer was evaluated with a "LEITZ" brand metallographic microscope equipped with a camera connected to a video tape recorder, and a ruler allowing the measurement.

The electrochemical measurements were conducted with an Autolab N128 Potentiostat, controlled by Nova software 1.7, in a three-electrode cell; the aluminum-based alloy as working electrode, a platinum sheet as counter electrode, and Ag–AgCl as the reference one (0.197 V vs. SHE). The polarization curves were performed at room temperature in aerated 3.5 wt.% NaCl solution, close to sea water ($\pm$ 150 mV), after OCP recording during 1 h, with 1 mV/s scan rate. A BioLogic SP-150 PGSTAT was used to achieve the electrochemical impedance spectroscopy (EIS) technique, in the range (1 MHz–1 mHz), with a perturbation amplitude of 10 mV around OCP.

3 Results and Discussions

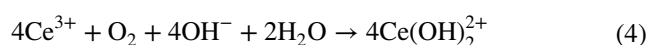### 3.1 Cerium-Conversion Coating Production by GCP methOd

Both Ce(OH)$_3$ ($K_s = 2.0 \times 0^{-20}$) and CeO$_2$ are poorly soluble and deposited from the precursor solution (0.1 M CeCl$_3$.7H$_2$O) owing to a local pH increase near the working electrode by OH$^-$ ions. This enrichment was provided by cathodic reduction of both dissolved O$_2$ (~ 8.26 mg/L, at 25 °C) and H$_2$O molecules. In addition, the non-reactivity of the chloride ions allows to the cerium ions to react with the produced OH$^-$ species leading to a better anticorrosive conversion deposit, in agreement with refs. [30, 31].

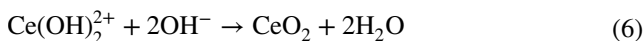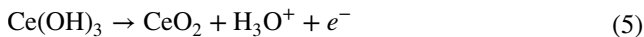(i) Formation of hydroxyl ions

$$O_2 + 2H_2O + 4e^- \rightarrow 4OH^- \tag{1}$$

$$2H_2O + 2e^- \rightarrow H_2 + 2OH^- \tag{2}$$

(ii) Cerium oxide/hydroxide production

$$Ce^{3+} + 3OH^- \rightarrow Ce(OH)_3 \tag{3}$$

$$4Ce^{3+} + O_2 + 4OH^- + 2H_2O \rightarrow 4Ce(OH)_2^{2+} \tag{4}$$

The products of reactions (Eq. 3) and (Eq. 4) may undergo oxidation and/or hydroxylation reactions, as stated by Eqs. (5) and (6):

$$Ce(OH)_3 \rightarrow CeO_2 + H_3O^+ + e^- \tag{5}$$

$$Ce(OH)_2^{2+} + 2OH^- \rightarrow CeO_2 + 2H_2O \tag{6}$$

3.2 Optimal operating parameters of the Ce-conversion deposit

Figure 1 shows the (log (i)vs.E) characteristics plotted after 1 h in contact with aerated 3.5 wt.% NaCl solution for specimens having undergone the CeEC process at different applied current densities for 5 min. It shows that the current density (i_{corr}) decreases firstly, signifying an improvement in the corrosion behavior, and then increases with the elaboration time, giving less-protective deposits. The curves (i_{corr} vs. time) plotted for different applied current densities (Fig. 1, Insert) establish that whatever the imposed density or the performing time, the corrosion behavior evolves in two stages. In the first one, the growth of the Ce-deposits blocks the cathodic zones formed by intermetallic particles, thus reducing the dissolution intensity, and leading to the improvement of the protection against corrosion. In the second step, the prolongation of the process beyond a critical time produces a thicker and less compact layer, which is more porous and consequently less adherent to the Al- substrate. The corrosion potential evolves from – 500 mV to a more negative value, less than—900 mV vs. Ag–AgCl,

indicating that the Ce-conversion coatings act rather as cathodic inhibitor.

Histograms in Fig. 2 exhibit the polarization resistances, calculated by the Stern-Geary equation (Eq. 7) [32].

$$R_p\left(\Omega.cm^2\right) = \left[2.303 i_{corr}\left(\frac{1}{b_a} + \frac{1}{b_c}\right)\right]^{-1} \tag{7}$$

where b_a (> 0) and b_c (< 0) are respectively the anodic and cathodic Tafel slopes ($dE/dlog(i)$), in (mV dec^{-1}) obtained by fitting the experimental data. Table 1 clearly reveals that the process of corrosion evolves kinetically from a cathodic control ($b_a < |b_c|$) associated to mass-transport limited oxygen reduction for the untreated substrate, toward the anodic control ($b_a > |b_c|$), for coated substrates.

The optimal operating parameters (OOP), corresponding to the best corrosion behavior, are observed for the conversion treatment at 5 mA/cm^2 and 5 min. Indeed, the polarization resistance (R_p) increases to reach a maximum value of 15.86 kΩ.cm^2, which is 4 times greater than that of the untreated specimen (2.65 kΩ.cm^2).

3.3 Study of the Synergistic Effect Between Anodizing Process and Ce-Conversion Deposit

The XRD patterns of the anodized and non-anodized samples (Fig. 3) having undergone a conversion deposit under OOP conditions confirms the ceria film coating of the CeO$_2$ phase. In fact, the apparition of eight peaks correspond to the Al substrate, crystallizing in the cubic system (SG: $m\bar{3}m$ – 225), with a lattice parameter $a = 4.056$ Å

Fig. 1 Log (i)vs.E curves plotted after 1 h in aerated 3.5 wt.% NaCl solution for specimens having undergone a CeCC process. Insert: (i_{corr} vs. time) curves for different applied current densities
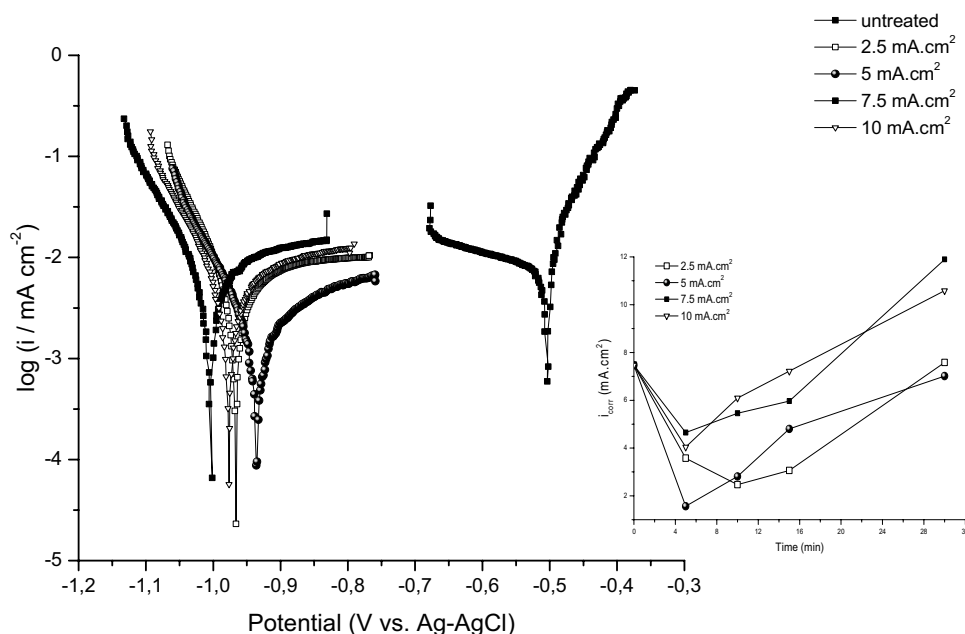
Fig. 2 Histograms of the calculated polarization resistance values
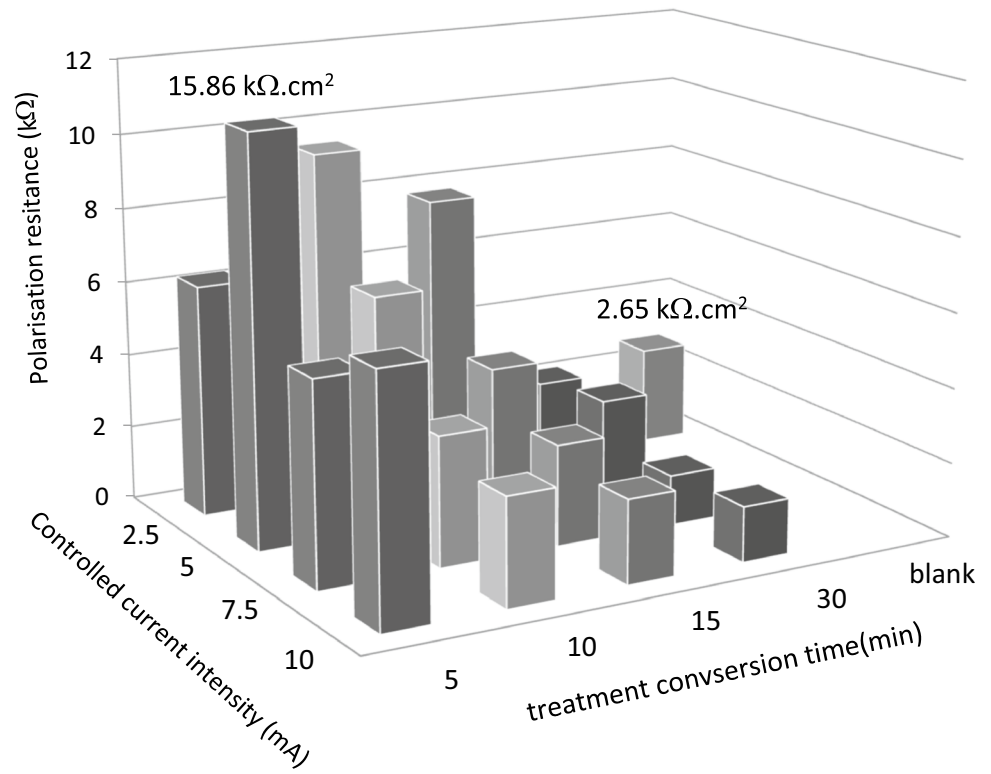
**Table 1** Electrochemical parameters of treated and untreated aluminum alloy specimens

Specimens	E_{cor} (mV)	i_{cor} (µA/cm^2)	b_c (mV.dec^{-1})	b_a (mV.dec^{-1})	R_p (kΩ cm^2)	EI (%)	$|Z|$ 0.001 Hz (kΩ cm^2)
Untreated	− 504	7.49	543	50	2.650	–	7.927
CeEC	− 935	1.60	81	210	15.86	78.63	10.05
An/CeEC	− 711	0.20	87	136	108.1	97.15	105.6

Fig. 3 The XRD patterns of the anodized and non-anodized samples treated with cerium conversion coating at 5 mA/cm^2 for 5 min
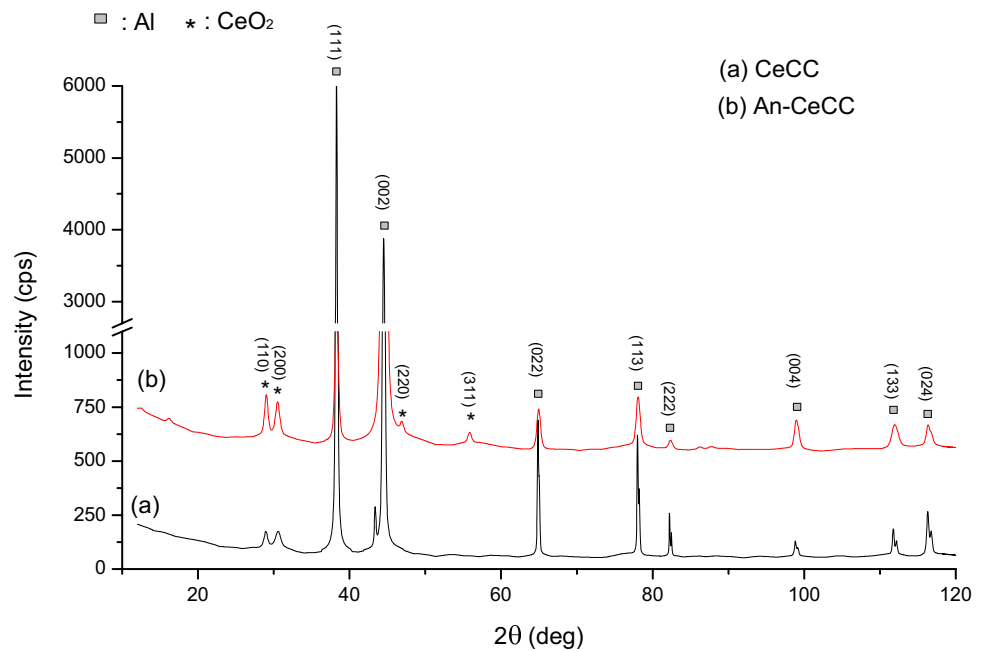
(JCPDS file N°01-072-3440). In addition, four other peaks at 29.01, 30.52, 44.10 and 55.86°, belonging to the cubic CeO_2 phase, correspond to (110), (200), (220) and (311) reticular plans with a fluorite type crystal structure and. It should be indicated that the peaks attributed to the CeO_2 structure are relatively broad indicating a semi-crystallinity. Furthermore, the diffractogram of aluminum sample treated according to CeEC treatment shows only the two most intense peaks located in the range (25°–30°). The Raman spectra (Fig. 4) enabled us to identify and confirm the formation of the solid phases based on cerium. Indeed, the spectra reveal the existence of a strong and dominated localized vibration band at 454 cm^{-1}, attributed to the well-known first-order optical mode (F_{2g}) of the symmetrical stretching of the Ce–O vibrational unit. Three other bands at 258, 603, and 1175 cm^{-1} with a weaker intensity are associated respectively to second-order transverse acoustic mode (2TA), defect-induced mode (D), and second-order longitudinal optical mode (2LO) [33, 34]. Furthermore, it can be easily seen an increase in the Raman intensity of the previously anodized specimen, owing to the existence of pores that have been clogged by cerium deposition. Examination of the optical micrographs (Fig. 5) of both anodized and non-anodized specimens' undergoing CeEC treatment reveals that the non-anodized one has a non-homogeneous morphology, with a partial overlap of the substrate surface. However, the cerium-based deposit made on the anodized Al-substrate is more homogeneous, covering almost the entire surface, with fewer defects. This result is clearly
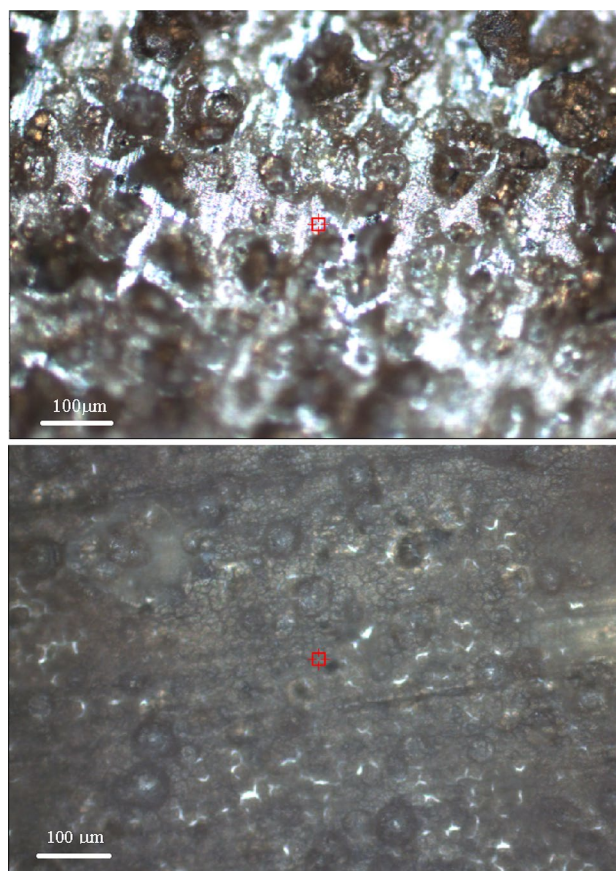
Fig. 5 Optical micrographs of both anodized and non-anodized specimens having undergone cerium conversion coating

Fig. 4 Raman spectra of anodized and non-anodized samples treated with cerium conversion coating
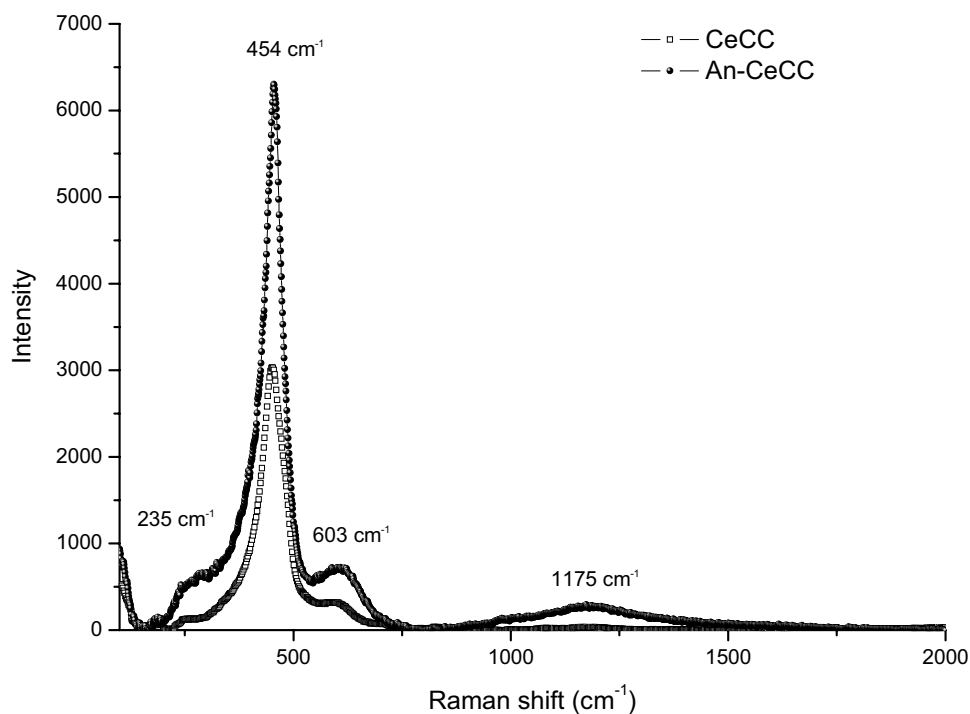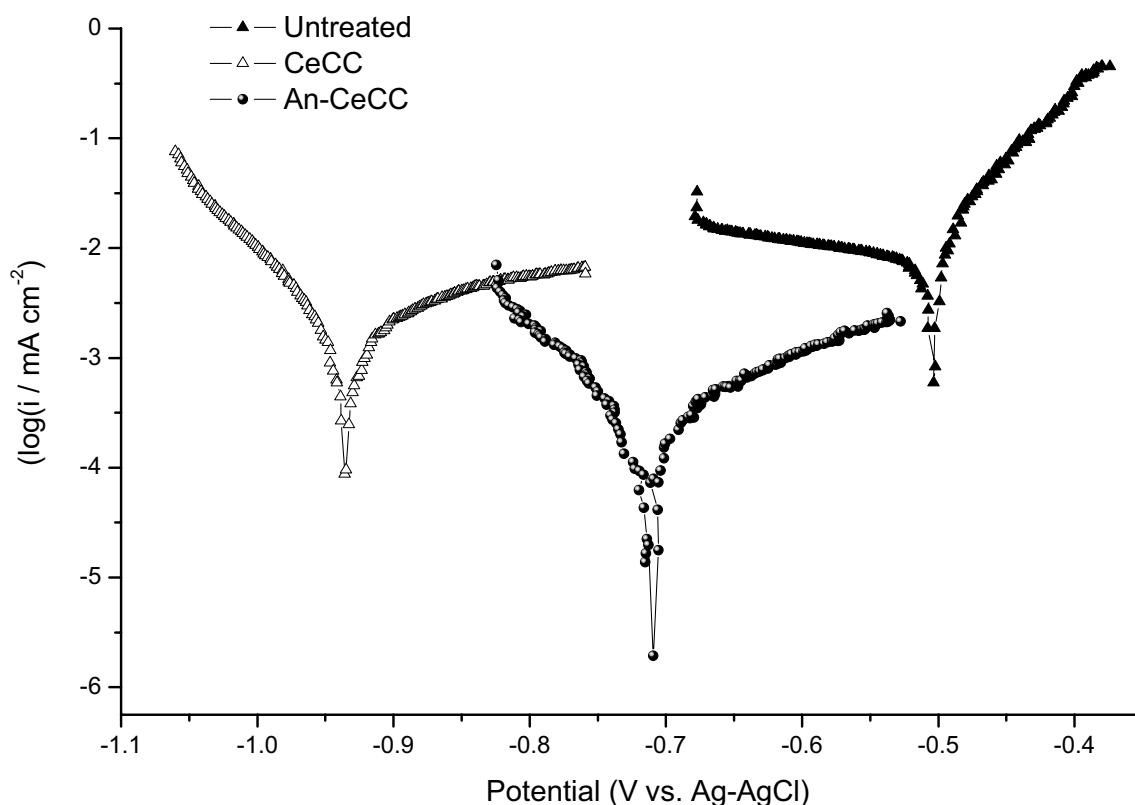
Fig. 6 Potentiodynamic polarization technique plots of untreated sample, and those treated according to CeCC and An-CeCC processes at 5 mA/cm² for 5 min

related to the existence of a higher porosity due to the anodizing process. The corrosion properties are studied in 3.5 wt.% NaCl solution, one of the most corrosive media. The selected semi-logarithmic (log (i) vs. E) plots (Fig. 6) clearly confirm the synergistic effect between the anodization process and the cerium conversion coating. Indeed, it exhibits a considerable improvement in the corrosion behavior of the aluminum alloy sample treated according to An/CeEC process. As stated by the electrochemical parameters exposed in Table 1, the polarization resistance (R_p) improves by more than 40 times (108.1 kΩ cm²) relative to the non-anodized sample (15.86 kΩ cm²), and their inhibiting efficiencies (*EI*), calculated according to Eq. (8) [35], are close to 97 and 78%, respectively.

$$EI(\%) = \left(1 - \frac{i_{corr}}{i_{corr}^0}\right) \times 100 \qquad (8)$$

where i_{corr} and i_{corr}^0 are the corrosion current densities of treated and untreated specimens, respectively.

The EIS plots (Fig. 7), recorded over a large frequency range (1 MHz–1 mHz) in 3.5 wt.% NaCl, clearly show distorted semicircles, revealing an outstanding anticorrosion properties for the specimen undergoing both anodizing and cerium-based conversion deposit, whose semicircle in the low frequency domain grows considerably, thus involving a stable anticorrosion barrier of CeO_2 compact protective film. Indeed, the corresponding Bode diagrams (log(Z) vs. log(f)) assert the well pronounced impedance, whose modulus is the highest over the entire frequency range (Fig. 7a, Insert), and evolves towards an almost stable value from 0.05 Hz frequency, in contrast to that of the CeEC-treated sample, which drops from 2.18 mHz. Besides, the low-frequency impedances at 0.001 Hz ($|Z|_{0.001}$) (Table 1), which can be assimilated to the polarization resistances for amply low frequency ($|Z|_{0.001Hz}(f \rightarrow 0) \approx R_p$), endorse those calculated using the Stern-Geary equation.

Furthermore, examination of the Phase (Z) vs. log(f) (Fig. 7b, Insert) reveals three time-constants for the untreated 2024 aluminum specimen, indicating three capacitive loops. The first loop involves the high-frequency double layer capacitance while the second one at medium frequencies, associates both the internal ionic charge-transfer resistance and bulk capacitance. The third loop is due to the faradic impedance combining both faradic-electron transferring resistance related to the corrosion process, and their corresponding low-frequency capacitance. In contrast, two time-constants are reported for the cerium-modified aluminum
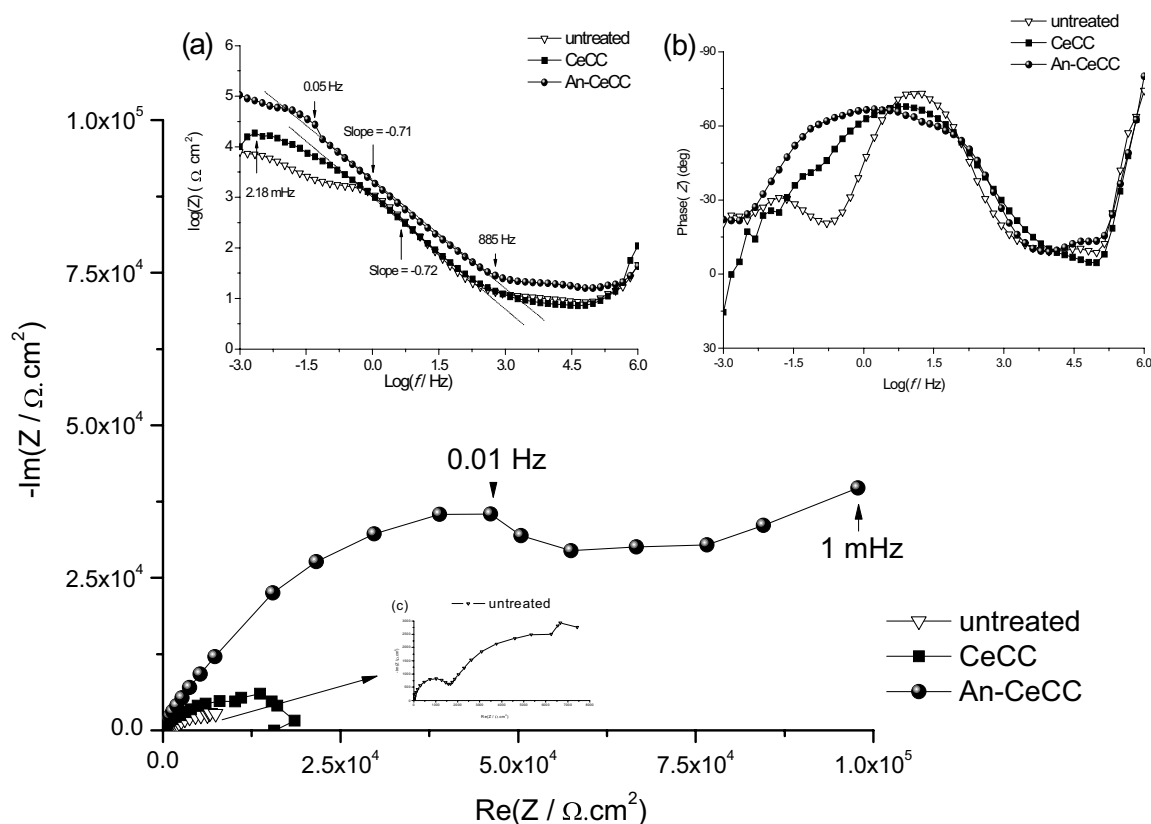
Fig. 7 Nyquist plots recorded in 3.5 wt.% NaCl in the frequency range (1 MHz–1 mHz). The corresponding Bode diagrams

specimens, linked respectively the high-frequency double layer capacitance and the medium–low frequencies impedance, involving the internal ion-diffusion through the oxide layer. Both the resistance and capacitance of the corrosion in low-frequencies, in agreement with previous obtained results for conversion deposits on 2024 aluminum alloy [36–39]. Commonly, the existence of a single broad-loop in the medium and low frequency domain (cf. Figure 7 b, Insert), which combines ionic and faradic processes, implies a "coalescence" between the reciprocal semicircles, whose characteristic frequencies are quite close, giving a single relaxation time [40, 41].

4 Conclusion

The synergistic effect efficiency between anodizing process and cerium-based conversion coating on the corrosion behavior of 2024 aluminum alloy substrate was successfully studied. The optimal operating parameters of the cerium conversion treatment, performed by galvanostatic cathodic polarization, are observed at a fixed current density of 5 mA/cm^2 for 5 min. The X-ray diffraction and Raman

spectroscopy confirmed the deposition of ceria (CeO_2) thin film, with a cubic fluorite type crystal structure. Moreover, the Raman study of the 2024 aluminum alloy undergoing both anodizing and cerium-based conversion deposit (An-CeEC) revealed a homogeneous deposit, covering almost the entire surface with fewer defects. Both polarization curves and EIS analysis showed the outstanding anticorrosion properties, owing to the synergistic effect giving rise to an efficient ion-barrier against the aggressiveness of the chloride-rich aerated environment (3.5 wt.%). The obtained polarization resistance (10^5 kΩ cm^2) and inhibiting efficiency (97%) were apparently greater than those of the solely cerium treated sample and the untreated one.

References

1. Martins NCT, Moura Silva T, Montemor MF, Fernandes JCS, Ferreira MGS (2008) Electrodeposition and characterization of polypyrrole films on aluminium alloy 6061–T6. Electrochim Acta 53:4754–4763

2. Ding H-Y, Dai Z-D, Skuiry S-C, Hui D (2010) Corrosion wear behaviors of micro-arc oxidation coating of Al_2O_3 on 2024Al in different aqueous environments at fretting contact. Tribol Int 43:868–875

3. Vargel C (2004) Corrosion of aluminium, 1st edn. Elsevier Science

4. Leblanc P, Frankel GS (2002) A Study of corrosion and pitting initiation of AA2024-T3 using atomic force microscopy. J Electrochem Soc 149(6):239–247

5. Li JF, Ziqiao Z, Na J, Chengyu T (2005) Localized corrosion mechanism of 2×××series Al alloy containing S(Al2CuMg) and θ'(Al2Cu) precipitates in 4.0% NaCl solution at pH 6.1. Mater Chem Phys 91(2005):325–329

6. Lacroix L, Blanc C, Pébère N, Thompson G, Tribollet B, Vivier V (2021) Simulating the galvanic coupling between S-Al_2CuMg phase particles and the matrix of 2024 aerospace aluminium alloy. Corros Sci 64:213–221

7. O'Keefe MJ, Geng S, Joshi S (2007) Cerium-based conversion coatings as alternatives to hex chrome: rare-earth compounds provide resistance against corrosion for aluminum alloys in military applications. Met Finish 105(5):25–28

8. IARC (2012) Arsenic, metals, fibres and dusts volume 100 C A review of human carcinogens, International Agency for Research on Cancer, World Health Organization, Lyons

9. U.S. Environmental Protection Agency (USEPA) (2016) Chromium in drinking water. Online: https://www.epa.gov/dwstandardsregulations/chromium-drinking-water. Accessed 20 Mar 2022

10. Forsyth M, Wilson K, Behrsing T, Forsyth C, Deacon GB, Phanasgoankar A (2002) Effectiveness of rare-earth metal compounds as corrosion inhibitors for steel. Corrosion 58(11):953–960

11. Wen Y-Q, Meng H-M, Shang W, Jiang X-J (2011) Electrochemical characteristics of the rare earth compound coating on 6061 aluminum alloy. Appl Mech Mater 71–78:2361–2365

12. Deyab MA, Abd El-Rehim SS, Hassan HH, Shaltot AM (2020) Impact of rare earth compounds on corrosion of aluminum alloy (AA6061) in the marine water environment. J Alloys Compd 820:153428

13. Hughes AE (2018). In: Klaus W (ed) Conversion coatings. Elsevier

14. Gulcovski J, Bajat J, Miscovic-Stankovic V, Jokic B, Panic V, Milonjic S (2013) Cerium oxide as conversion coating for the corrosion protection of aluminum. J Electrochem Sci Eng 3(4):151–156

15. Castano CE, O'Keefe MJ, Fahrenholtz WG (2015) Cerium-based oxide coatings. Curr Opin Solid State Mater Sc 19(2):69–76

16. Wang C, Jiang F, Wang FY (2004) Cerium chemical conversion coating for aluminum alloy 2024–T3 and its corrosion resistance. Corrosion 60(3):237–243

17. Harvey TG (2013) Cerium-based conversion coatings on aluminium alloys: a process review. Corros Eng Sci Techn 48(4):248–269

18. Lu C, Mu S, Du J, Zhang K, Guo M, Chen L (2020) Investigation on the composition and corrosion resistance of cerium-based conversion treatment by alkaline methods on aluminum alloy 6063. RSC Adv 10:36654–36666

19. Johansen HD, Brett CMA, Motheo AJ (2012) Corrosion protection of aluminium alloy by cerium conversion and conducting polymer duplex coatings. Corros Sci 63:342–350

20. Valdez B, Kiyota S, Stoytcheva M, Zlatev R, Bastidas JM (2014) Cerium-based conversion coatings to improve the corrosion resistance of aluminium alloy 6061–T6. Corros Sci 87:141–149

21. Luo Y-R, Byrne RH (2007) The influence of ionic strength on yttrium and rare earth element complexation by fluoride ions in NaClO4, NaNO3 and NaCl solutions at 25 °C. J Solut Chem 36:673–689

22. Kikuchi T, Suzuki Y, Iwai M, Suzuki RO (2020) Anodizing aluminum and its alloys in etidronic acid to enhance their corrosion resistance in a sodium chloride solution. J Electrochem Soc 167:121502

23. Wang R, Wang L, He C, Lu M, Sun L (2019) Studies on the sealing processes of corrosion resistant coatings formed on 2024 aluminium alloy with tartaric-sulfuric anodizing. Surf Coat Technol 360:369–375

24. Yu S, Wang L, Wu C, Feng T (2019) Studies on the corrosion performance of an effective and novel sealing anodic oxide coating. J Alloys Compd 817:153257

25. Canyook R, Seubsom P, Sang-ngean J, Trirujirapapong T, Taweesup K (2018) Influences of sealing solutions on anodized layer properties of 7075 aluminium alloy. Mater Today Proc 5(3):9483–9488

26. Kikuchi T, Suzuki Y, Iwai M, Suzuki RO (2019) Corrosion-resistant porous alumina formed via anodizing aluminum in etidronic acid and its pore-sealing behavior in boiling water. J Electrochem Soc 166:261–269

27. Priet B, Odemer G, Blanc C, Giffard K, Arurault L (2016) Effect of new sealing treatments on corrosion fatigue lifetime of anodized 2024 aluminium alloy. Surf Coat Technol 307:206–219

28. Castro Y, Özmen E, Durán A (2020) Integrated self-healing coating system for outstanding corrosion protection of AA2024. Surf Coat Technol 387:125521

29. Catalina F, Rueda G, Gonzalez JT (2020) Electrochemical polymerization of polypyrrole coatings on hardanodized coatings of the aluminum alloy 2024–T3. Electrochim Acta 347:136272

30. Arurault L, Monsang P, Salley J, Bes RS (2004) Electrochemical preparation of adherent ceria coatings on ferritic stainless steel. Thin Solid Films 466:75–80

31. Creus J, Brezault F, Rebere C, Gadouleau M (2006) Synthesis and characterisation of thin cerium oxide coatings elaborated by cathodic electrolytic deposition on steel substrate. Surf Coat Technol 200:4636–4645

32. Obot IB, Ankah NK, Sorour AA, Gasem ZM, Haruna K (2017) 8-Hydroxyquinoline as an alternative green and sustainable acidizing oilfield corrosion inhibitor. SM&T 14:1–10

33. Wu Z, Li M, Howe J, Meyer HM III, Overbury SH (2010) Probing defect sites on CeO_2 nanocrystals with well-defined surface planes by Raman spectroscopy and O_2 adsorption. Langmuir 26(21):16595–16606

34. Spanier JE, Robinson RD, Zheng F, Chan SW, Herman IP (2001) Size dependent properties of CeO_{2-y} nanoparticles as studied by Raman scattering. Phys Rev B 64(24):245407

35. Ye Y, Zou Y, Jiang Z, Yang Q, Chen L, Guo S, Chen H (2020) An effective corrosion inhibitor of N doped carbon dots for Q235 steel in 1M HCl solution. J Alloys Compd 815:152338

36. Saillard R, Viguier B, Odemer G, Pugliara A, Fori B, Blanc C (2018) Influence of the microstructure on the corrosion behaviour of 2024 aluminium alloy coated with a trivalent chromium conversion layer. Corros Sci 142:119–132

37. Stoica A-I, Świątowska J, Romaine A, Di Franco F, Qi J et al (2019) Influence of post-treatment time of trivalent chromium protection coating on aluminium alloy 2024–T3 on improved corrosion resistance. Surf Coat Technol 369:186–197

38. Zheludkevich ML, Yasakau KA, Bastos AC, Karavai OV, Ferreira MGS (2007) On the application of electrochemical impedance spectroscopy to study the self-healing properties of protective coatings. Electrochem Commun 9:2622–2628

39. Zheludkevich ML, Serra R, Montemor MF, Yasakau KA, Miranda Salvado IM, Ferreira MGS (2005) Nanostructured sol–gel coatings doped with cerium nitrate as pre-treatments for AA2024-T3 Corrosion protection performance. Electrochim Acta 51:208–217

40. Trémillon B (1997) Analytical electrochemistry and reactions in solution. Wiley, Berlin

41. Lvovich VF (2012) Impedance spectroscopy: applications to electrochemical and dielectric phenomena. Wiley